Acta Materialia 113 (2016) 19–31

Contents lists available at ScienceDirect

Acta Materialia

journal homepage: www.elsevier.com/locate/actamat

Full length article

Vessel microstructure design: A new approach for site-specific core-shell micromechanical tailoring of TRIP-assisted ultra-high strength steels

M. Belde*, H. Springer, D. Raabe

Max-Planck-Institut für Eisenforschung GmbH, 40237 Düsseldorf, Germany

ARTICLE INFO

Article history:
Received 2 March 2016
Received in revised form
21 April 2016
Accepted 24 April 2016

Keywords:
TRIP-Assisted steel
Composite
Microstructure design
Strength
Uniform elongation

ABSTRACT

The mechanical performance of multi-phase steel microstructures critically depends on the constituents' chemical and morphological constitutions, which in combination determine the composite hardness, the onset of plasticity, internal load and strain-partitioning, as well as the stability and transformation kinetics of retained austenite in case of TRIP steels. The novel approach of utilising temporary vessel phases, hence termed vessel microstructure design, enables the tuning of constituent phase properties by linking their formation to a controllable landscape of chemical gradients. This approach hinges on the introduction of alloy carbides as a temporary container, or 'vessel' phase, deliberately producing localised enrichment of alloying elements in a structure predetermined by preliminary heat treatments, referred to as conditioning and accumulation stages. These vessel carbides, which act as reservoirs for specific alloying elements, are then partially dissolved through flash heating, leading to a self-organising landscape of alloying elements in the vicinity of the dissolving particles. The resulting three- or multiple phase microstructures then consist of confined laminates incorporating retained carbides, enveloped by retained austenite shells, embedded within a martensitic matrix. Such complex yet entirely self-organized microstructures offer unique opportunities for strain and load partitioning which we refer to as core-shell micromechanics. Different variants of these core-shell composite structures are produced and examined together with reference microstructures by tensile testing, hardness mappings, impact toughness, X-ray measurements, as well as by electron microscopy. It is found that these novel microstructures, when tempered, exhibit ultra-high strength and delayed necking, enabled by a combination of gradual strain-hardening and transformation-induced plasticity that is tuneable via control of the initial carbide structure.

1. Introduction

Advanced high strength steels (AHSS) are developed for both outstanding mechanical properties, and, increasingly, for austerity in strategic alloying additions ('lean alloys') [1,2]. Mainly driven by the automotive and manufacturing industries [3], these steels are continuously improved, towards increasing passenger safety and fuel economy while reducing manufacturing costs at the same time. Towards these goals, AHSS offer efficient optimisation strategies in the form of blended microstructures, where mixing and tuning constituents offers synergistic property design. Metastable austenite is an especially attractive constituent, due to its propensity for transformation-induced plasticity (TRIP [4]) that may contribute strain-hardening reserves for delaying plastic instability [5–7] and for arresting or blunting cracks that would otherwise easily propagate through the surrounding martensite [8,9]. Classic examples of its use are first generation AHSS TRIP-steels, where austenite is stabilised during step-quenching into the bainite regime (austempering) by the influx of carbon (C) into austenite from adjoining sheaths of bainitic ferrite. This concept yields attractive TRIP-assisted properties, but is capped in terms of strength (800–1000 MPa [10]) by the predominantly ferritic matrix. Third generation AHSS TRIP-steels avoid this shortcoming by exchanging bainite and ferrite for much stronger martensite, which is achieved by simply lowering the quench temperature to below the martensite start temperature M_S, resulting in so-called

* Corresponding author.
E-mail address: m.belde@mpie.de (M. Belde).

http://dx.doi.org/10.1016/j.actamat.2016.04.051
1359-6454/

quenching and partitioning (Q&P) steels. In this manner, ultimate tensile strengths may be increased to about 1300 MPa, while remaining within the same range of alloying (medium C, about 1–3Mn and Si [10]). The deliberate lowering of the quench temperature is the cornerstone of the Q&P treatments [11], which has been recognised as the only method to stabilise austenite for low C-contents [12], critically satisfying the goal of alloying austerity in addition to high strength. The Q&P process has recently also been applied to stainless steel grades AISI 410 [12] and AISI 420 [13]. For still higher alloying additions, and lower M_S temperatures, the partitioning process was shown to be pertinent in a two-step quenching and tempering (Q&T) variant as well [8,14]. In both, Q&P and Q&T, the martensite fraction has to undergo significant and unavoidable softening during the necessary holding time at elevated temperature (typically situated at 400–450 °C) during the partitioning step [6,12,15], thus also limiting overall attainable strength.

Austenite obtained through partitioning is determined by the quench temperature in terms of its chemical composition, which is inversely related to its volume fraction, in accordance with the constrained carbon equilibrium (CCE) model, assuming full partitioning and homogeneous C-concentrations within martensite and austenite [12,16]. Furthermore, austenite stabilised by partitioning treatments is frequently characterised as of lamellar, film-type morphology [8,16,17], as determined by its inter-lath morphology. Austenite derived from bainitic holding, on the other hand, is reported as conforming to a more insulated and granular morphology [18,19]. While substitutional alloying additions may generally alter austenite appearance [14], the processing typically exerts a controlling influence on its shape and distribution, which is of crucial importance for tailoring its effect on the mechanical properties of the bulk steel [3,20], thus limiting control over its optimisation.

In a martensitic-austenitic microstructure, ductility and damage resistance rest mainly on the performance of the respective austenite fraction in terms of stability, size, dispersion and composition, thus rendering its optimisation the most critical avenue for design towards optimised mechanical properties [21,22]. To this end, avoiding premature (i. e. stress-induced [8]) or autocatalytic ("burst-like") transformation [23], and instead attaining a gradual, consistent and beneficial TRIP-effect is of prime importance [6,24].

A graded distribution of stabilities over individual austenite grains is needed to avoid such monolithic transformation effects, typically associated with overly uniform character distributions within the austenite fraction, such as high connectivity or common texture, similar size or C-concentrations [3,9,25]. Thus, designing an ideal austenite constituent, comprising isolated particles of graded composition, as well as tuneable morphology and size, to guarantee a gradual benefit to strain-hardening via an optimised TRIP-effect, is outside the scope of conventional "top-down" processing. Towards attaining this goal, a new "bottom-up" processing approach was recently proposed by the current authors, here proposed to be termed "Vessel Microstructure Design" (VMD) [26]. It was demonstrated that $M_{23}C_6$ alloy carbides in medium C stainless steel (corresponding to AISI 430/Fe–12Cr–0.3C) may be exploited as a temporary vessel (i.e. container-type) phase, chemically stabilising retained austenite, to produce a novel core-shell-type morphology around partially dissolved carbides upon flash heating (in a principle previously reported on as an isolated feature in literature [27–29]). It was also shown that the carbide morphology and dispersion can be inherited to the enveloping austenite, essentially allowing microstructure design by proxy through the easily tuned processes of carbide precipitation and growth [26]. The final carbide dissolution process, on the other hand, can be used to tune chemical gradients within the austenite, as well as to promote overall grain refinement and orientation multiplicity. As such, the new microstructure combinations obtainable through VMD processing are attractive candidates for further and more in-depth study pertaining to their mechanical performance.

2. Objective

The objective of this work is to explore the performance of novel microstructure blends enabled by VMD processing in respect to the mechanical properties associated with their novel core-shell type microstructures. The mechanical properties are compared to those of reference quenched and tempered martensite microstructures with special attention paid to the TRIP-effect, the connected austenite properties, and the micromechanical core-shell particles themselves.

3. Experimental

The Fe–12Cr alloys with nominal C concentrations of 0.2 and 0.3 wt.%, respectively, were produced by vacuum induction melting, cast into a copper mould, subsequently rolled at 1100 °C in 8 passes from 40 to 3.5 mm thickness and air-cooled to room temperature. From the rolled sheets slabs of 20 × 60 × 3.5 mm^3 were cut by spark erosion and heat-treated in horizontal glass tube muffle furnaces under protective argon atmospheres. These heat treatments, referred to as conditioning (homogenisation at 1150 °C) and accumulation (soft-annealing at 750 °C) stages, were varied in the way previously described elsewhere [26], as sketched in Fig. 1a, to produce several distinct vessel carbide microstructures. The

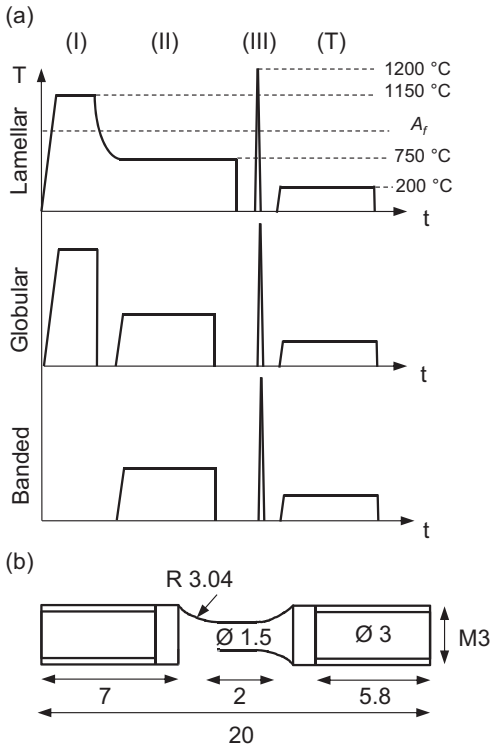

Fig. 1. (a) Schematic showing the modular combination of varied (I) Conditioning and (II) Accumulation stages to obtain three unique types of vessel-designed microstructures after (III) Dissolution. Optional posterior tempering (T) is also sketched. Processing parameters are compiled in Table 1, A_f refers to the austenite start temperature. (b) Custom cylindrical tensile specimen geometry, necessitated by compliance with dilatometer heating.

respective thermal histories and designations of all sample states are compiled in Table 1.

The different ferrite-carbide microstructures produced in this manner are henceforth referred to as being of type Globular, Banded, or Lamellar. According to inductively coupled plasma optical emission spectrometry (ICP-OES) analysis, performed on selected samples after each of these preliminary heat treatments, aluminium, silicon, manganese, nickel and nitrogen are all below 0.01 wt.%, phosphorous below 0.002 wt.%. The different sampled states contain within 11.6 (LC) to 12.5 wt.% Cr (HC), where the extensions LC and HC in Table 1 stand for low C (0.22–0.24 wt.%) and high C (0.32 wt.%), respectively. From the thus treated slabs, cylindrical tensile samples with a gauge length of 2.0 mm and a loaded cross section of 1.5 mm diameter (Fig. 1b) were prepared using a combination of spark erosion and turning lathe. This custom geometry was selected to comply with subsequent dilatometer processing. The last processing stage, termed dissolution (flash heating to 1200 °C), aims at partially dissolving the vessel-carbides through rapid heating, in order to promote shells of retained austenite. These transient heat treatments were performed on individual tensile specimens, using a Bähr Dil805 dilatometer, equipped with induction heating, under a vacuum of 4×10^2 Pa. Heating and cooling rates were set to be 200 °C s^{-1} with holding times of 1 or 3 s at temperatures of 1200 °C. Quenching to room temperature was carried out by helium gas. Posterior tempering for 20 min at 100, 200, 300, and 400 °C was applied also in the dilatometer. Reference samples did not undergo accumulation treatment and were instead only subjected to conditioning, and in part to dissolution, before subsequently being tempered at 200 or 400 °C, in order to produce reference structures of low-tempered martensite or C-partitioning, respectively (Table 1).

The heat-treated tensile samples were tested in a Kammrath & Weiss GmbH setup via two dimensional digital image correlation measurements (DIC), using Aramis software, version 6.3.0-6 © 2011 GOM mbH, at a strain rate of 0.5^{-3} s^{-1}. Microstructures were characterised post-mortem on embedded samples, grinded to half thickness, exposing longitudinal cross-sections. After grinding followed polishing with 1 μm grained diamond suspension on lubricated cloth discs. Final polishing for all subsequent characterisation was obtained using colloidal silica (50 nm) suspension. Microhardness was probed using a Fischerscope® HM2000 microindenter with a Vickers diamond tip scanning a grid of 15 × 15 measurement points in a step size of 10 μm at loads of 100 mN. 15 J impact toughness was evaluated on 27 × 4 × 3 mm^3 samples, round-notched at radius 3 mm. In this case the dissolution treatment was performed in a liquid tin bath held at a temperature of 1140 °C, followed by water quenching and tempering at 200 °C for 20 min under air.

XRD phase quantification was obtained using Rietveld analysis on spectra supplied by Huber 2-Circle goniometers, equipped with energy dispersive Meteor0D point detectors, using Co K_α radiation. Rietveld analysis was done using MAUD software (version 2.33, 2010) [30]. XRD measurements of higher spatial resolution were performed within the tensile sample gauge lengths using a Bruker D8 Advance, equipped with an area detector, with a spot of 1 mm. In this case, quantification was derived from the relative integrated intensities of 111_γ, 110_α, and 200_γ peaks, according to Jatczak [31]. Electron back-scatter diffraction (EBSD) was performed using a JEOL JSM 6500 microscope, equipped with EDAX EBSD systems and TSL OIM software with a step size of 50 nm at 15 kV, disregarding all data possessing a confidence index below 0.1. Correlative nano-indentation was carried out using a Hysitron TriboIndenter, equipped with a Ti 39-1 Bercovich tip at a constant load of 300 μN.

4. Results

4.1. Core-shell microstructures

Three fundamental vessel-designed microstructures and two C-concentrations form the basis of the subsequent characterisation and mechanical evaluation. The three types of VMD morphologies are based on identical flash-heating of different ferrite-carbide microstructures, represented in Fig. 2a by SEM micrographs. These types of microstructure are referred to as (from left to right) Lamellar, Globular, and Banded after their carbide – and subsequently – austenite (green) morphologies, presenting in the so-called core-shell particles. These microstructures, made up of different core-shell structures, stem from three modular arrangements of the preliminary conditioning and accumulation steps (i. e. vessel preparation) previously presented in Fig. 1a and Table 1. The globular morphology, tested as low and high C variants, is achieved by separate homogenisation and accumulation treatments, incorporating relatively fine and evenly dispersed carbides, nucleated and grown in as-quenched martensite during aging after reheating. By contrast, the lamellar morphology (low C only) is produced by linking both treatments via furnace cooling, thus employing discontinuous carbide precipitation during the $\gamma \rightarrow \alpha$ phase transformation, resulting in needle-shaped and grain boundary carbides of strongly varied sizes. The accumulation stage is extended (from 47 to 70 h) to compensate for the absence of martensite, which is otherwise facilitating a higher mobility of substitutional Cr, necessary to quickly achieve the high local enrichments inherent to $M_{23}C_6$ of equilibrium composition [26]. The banded morphology (high C only) forgoes homogenisation entirely, instead making use

Table 1
Table compiling the different sample states subjected to microstructure analysis, micro-hardness and tensile testing together with their C-content (low C-content: LC, high C-content: HC) and processing stages. The samples are divided into Vessel Microstructure Design (VMD: Subjected to Conditioning, Accumulation, Dissolution and containing alloy carbides) and reference states (free from alloy carbides due to lack of Accumulation treatment, subjected to Dissolution only in case of the VMD Martensite reference). Samples of type Globular LC were examined by nano-indentation and in impact toughness tests. GC, FC, OQ denote quenching modes by helium gas in the dilatometer, furnace cooling, or oil quenching, respectively. C-contents were measured on fully processed tensile specimens post-mortem by ICP-OES, the Cr-contents are comparable between 11.6 and 12.5 wt.%.

Processing	Designation	C-content [wt.%]	Conditioning	Accumulation	Dissolution	Posterior tempering, GQ
			1150 °C	750 °C, OQ	1200 °C, GQ	
Vessel microstructure design	Lamellar LC	0.23	2 h, FC	70 h	1 s/3 s	200 °C, 20 min
	Globular LC	0.24	2 h, OQ	47 h	1 s/3 s	100/200/300/400 °C, 20 min
	Globular HC	0.32	2 h, OQ	47 h	3 s	200 °C, 20 min
	Banded HC	0.32	as-rolled	47 h	1 s/3 s	200 °C, 20 min
Reference states	Q&T LC	0.22	2 h, OQ	–	–	400 °C, 30 min
	Martensite LC	0.23	2 h, OQ	–	–	200 °C, 20 min
	VMD LC	0.22	2 h, OQ	–	3 s	200 °C, 20 min
	Martensite HC	0.32	0.5 h, GQ	–	–	200 °C, 20 min

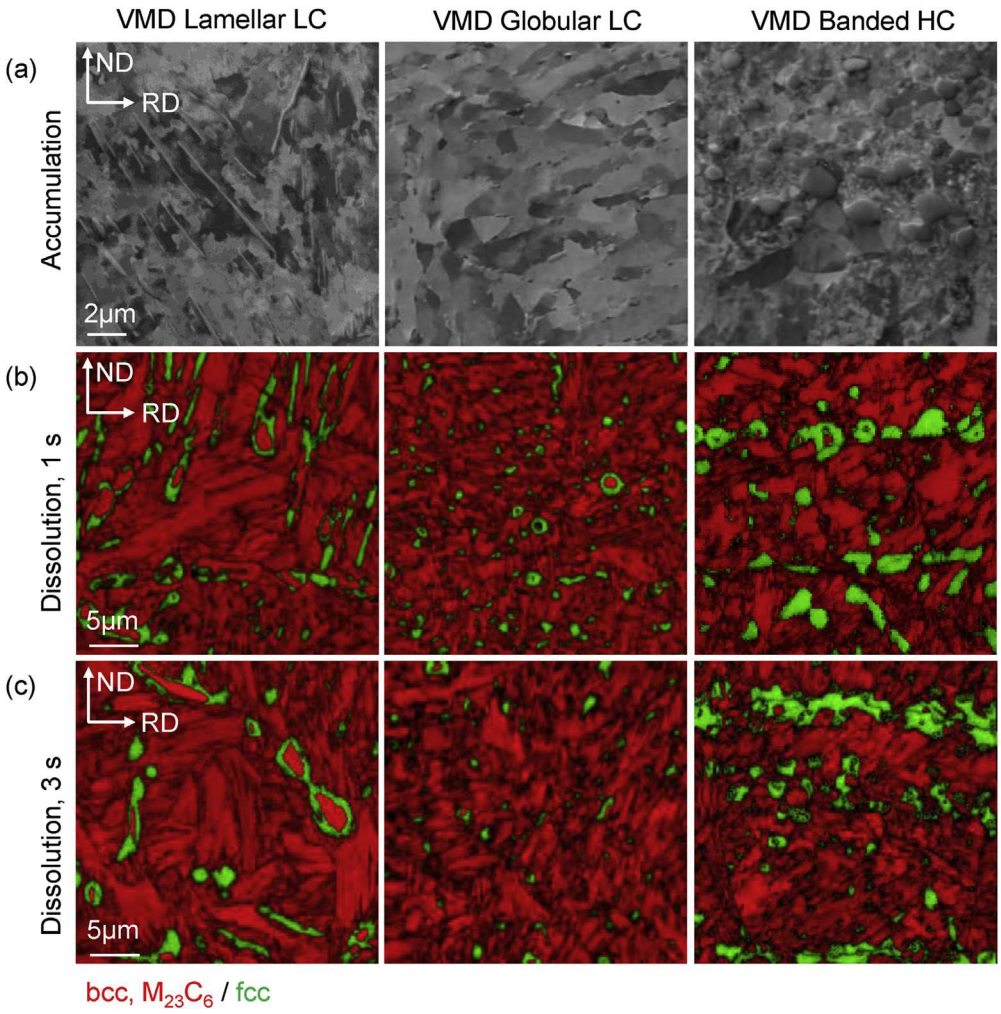

Fig. 2. (a) SEM micrographs, highlighting the three different "as-accumulated" ferrite-carbide microstructures prior to flash heating, left to right: Lamellar, Globular, Banded. Below, representative EBSD results show "as-dissolved" microstructures in merged phase and image quality mappings after (b) 1 s holding and (c) 3 s holding at 1200 °C, followed by gas-quenching. The residual carbides within austenite shells cannot be reliably indexed, but are distinguishable by their high uniform image quality. The initial pronounced differences in carbide size and morphology can be observed to transfer over to the retained austenite.

of rolling-induced segregation planes for a preferential arrangement of carbides that are also comparatively larger (micron-sized). The final dissolution steps, applied to introduce austenite, are identical in all cases, but lead to pronounced differences in retained austenite morphology, in accordance with their shapes being inherited from the respective vessel carbides, previously imprinted by the respective processing. Examples are shown for the two selected holding times, namely 1 s and 3 s at 1200 °C, as EBSD maps in Fig. 2b and c, respectively. The micrographs reveal residual carbides (in red, distinguishable by their high image quality) and their enveloping shell of retained austenite (green) form a novel type of core-shell composite microstructure. Thermo-Calc gives the carbide volume fractions prior to dissolution as about 6.2 vol.% for low and 3.9 vol.% for high C variants, respectively. The XRD austenite fractions, resulting from the partial dissolution of these carbide fractions, are, in vol.% from left to right, for 1 s (3 s) holding: 8.0 (7.0), 4.9 (5.8), 12.1 (10.4) for Lamellar to Banded. The attained austenite grain sizes generally correlate with the previous mean carbide diameter, thus being larger for Banded and Lamellar and smallest for Globular microstructures (Fig. 2a). Increasing the dissolution time from 1 to 3 s increases the mean austenite grain sizes (equivalent diameter) as calculated by OIM EBSD software: Banded 470 ± 470 nm to 810 ± 320 nm; Lamellar: 430 ± 480 nm to 920 ± 280 nm; Globular 360 ± 300 nm to 880 ± 270 nm. Regarding the volume fraction, XRD shows no strong change accompanying this development. The C-content and resultant carbide fraction is not strictly correlated with attainable levels of retained austenite, but seems to be rather a product of the respective carbide microstructures. For a more detailed description of VMD as pertaining to chemical gradients, stabilising austenite locally via M_S temperature depression, as well as the kinetic exploitation by processing, the reader is referred to a previous paper dedicated to these subjects [26].

4.2. Posterior tempering

The microstructures compiled in Fig. 2, as-quenched from 1200 °C, showed ultra-high strength but a lack of tensile ductility (AQ in Fig. 3). Posterior tempering was therefore applied in the range of 100–400 °C, the resulting properties of which are compiled in Fig. 3. The error bars denote standard deviations from a mean of several specimens; the chosen microstructure in this case is Globular LC. Tempering leads to the best combination of properties in the range of 200 °C, at only minor detriment to the very high tensile strength (UTS) and hardness (HV), the total and uniform elongations (TE, UE) are substantially increased, combined

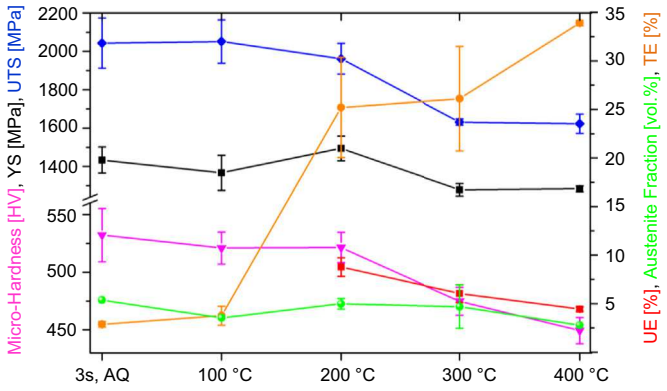

Fig. 3. Evolution of tensile properties, micro-hardness and austenite fraction (measured by XRD Rietveld analysis) with posterior tempering treatments, changing at temperature increments of 100 °C, applied for 20 min, followed by gas-quenching, on the basis of the as-quenched (AQ) condition, previously held for 3 s at 1200 °C. The error bars denote standard deviations around the respective means of several specimens of type Globular LC. YS: Off-set yield strength, UTS: Ultimate tensile strength, UE: Uniform elongation, TE: Total elongation to fracture.

with a somewhat higher yield point (YS). The austenite volume fraction, as measured by XRD, shows no significant change up to 400 °C, but necking accelerates above 200 °C.

Tempering at 200 °C was selected for more in-depth analysis in the following, as it clearly shows the best compromise between strength and ductility. Three representative VMD product microstructures of this treatment are compiled in Fig. 4 (columns 1 to 3), showing no significant differences to the corresponding non-tempered states (Fig. 2). Further mechanical testing also incorporated two conventionally treated reference conditions (Fig. 4, columns 4 and 5): alloy carbide free and chemically homogeneous [26] low temperature tempered martensite (LTT [32], partially additionally flash heated to produce reference state VMD, see Table 1) and a quenched and tempered (Q&T [14,33,34]) state aimed at C-partitioning (see reference state Q&T Table 1). EBSD maps (Fig. 4, 1st row) highlight familiar austenite morphologies and dispersions for the VMD variants, while the reference states (at the same 0.2 wt.% C) are characterised by only very minor austenite fractions (reference state Q&T, about 2 vol.%) and its complete absence (VMD and low C martensite reference states). Furthermore, inverse pole figure (IPF) mappings highlight the (prior austenite) grain size and subsequent orientation multiplicity for austenite via texture memory (Fig. 4, 2nd row), as well as martensite and residual carbides (Fig. 4, 3rd row). It is evident that in case of VMD-processed specimens, especially Globular and Banded, the dissolution stage leads to considerable refinement of prior austenite grains and increase in orientation multiplicity, whereas in the absence of alloy carbides it is much less affected. By way of comparison, the

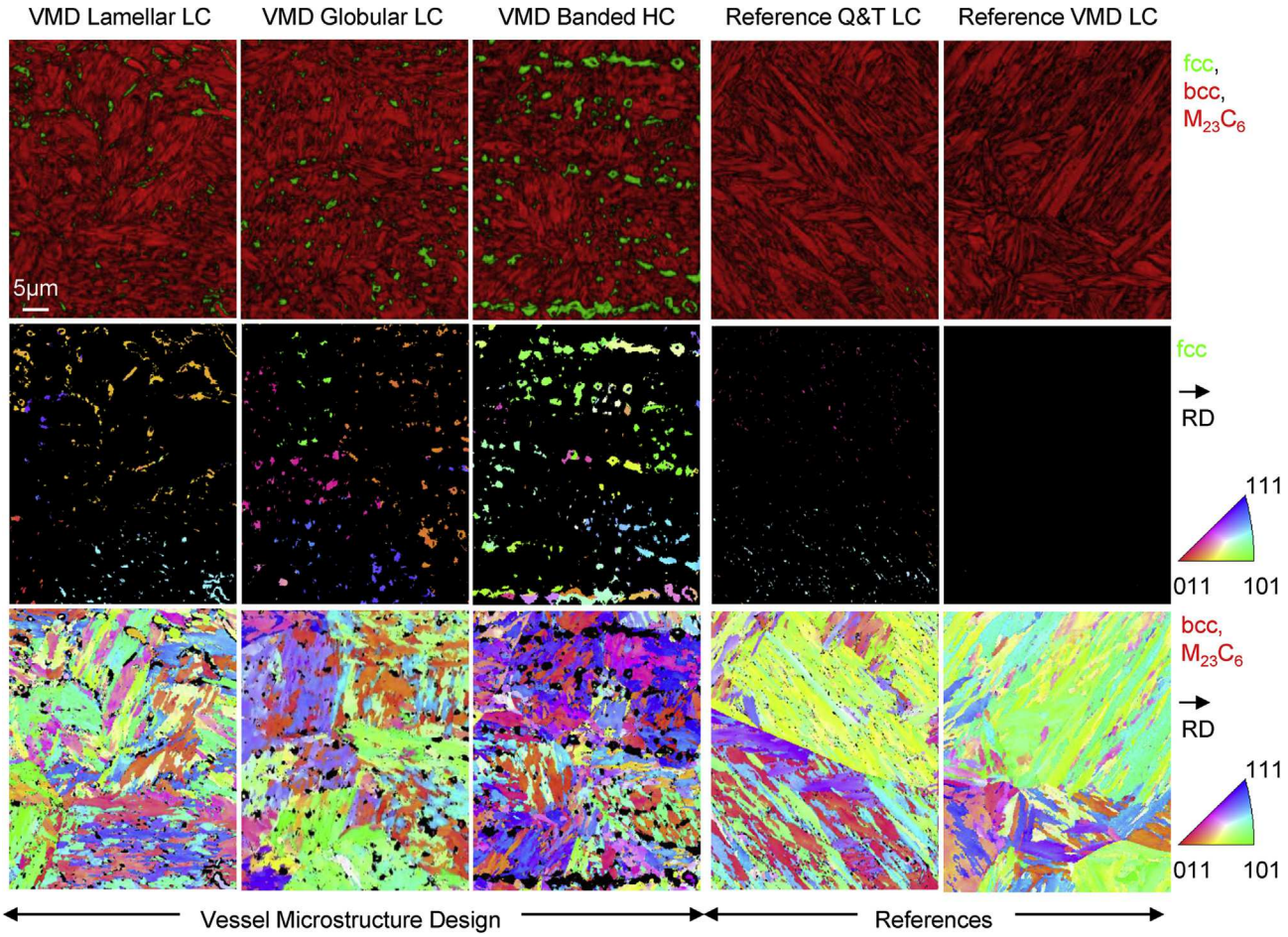

Fig. 4. EBSD mappings highlighting the main microstructures subjected to mechanical testing in merged phase and image quality map (1st row), and inverse pole figure map for austenite (2nd row) and matrix plus carbide (3rd row), for Vessel Microstructure Design and two reference microstructures. The inverse pole figure mappings show retained austenite grain size and texture memory (2nd row) as well as underlying prior austenite grain size (3rd row) and its change by structural refinement due to flash heating, applied equally, except for low carbon Q&T reference, which shows the unchanged, as-homogenised and tempered structure.

reference state Q&T still exhibits the as-homogenised grain size condition also representative of the martensitic reference state. Whether or not as-homogenised martensite (i.e. the LC martensitic reference state) is additionally subjected to flash-heating (3 s at 1200 °C, turning it into the carbide-free VMD reference state) thus only slightly changes the grain size characteristics in the absence of $M_{23}C_6$ carbides. According to the EBSD analysis, the grain boundary density per unit length increases from 1.2 to 1.6 at martensite grain diameters of 640 ± 220 nm and 610 ± 117 nm, respectively. By comparison, the relative boundary density is 2.3 in case of Globular VMD.

4.3. Mechanical characterisation

Representative engineering stress-strain curves of the five studied VMD and reference microstructures are presented in Fig. 5 along with their total mean XRD austenite fraction, separated by C-content into (a) LC and (b) HC for different microstructures, as well as (c) for different dissolution times (compare Fig. 2b,c, 2nd row). In Fig. 5a, VMD Globular LC (red) presents an average UTS of 1961 ± 80 MPa and UE of 8.8 ± 1.0% over all tested specimen. This strength conforms to flash-heated and tempered martensite (reference state VMD LC in Table 1, continuous grey line) while exceeding that of the non-flash-heated reference martensite (dashed grey line). The accompanying YS of 1494 ± 68 MPa (red) is also comparable to that of martensite, while the effect of strain-hardening is initially weaker for the VMD microstructures, as compared to monolithic martensite, with strain it is increasing and outlasting it. The reference state Q&T (orange) is comparable to reference martensite in this respect of strain-hardening, but shifted downwards by about 400 MPa and reaching much higher post-necking elongations. Lamellar VMD shows, compared to Globular VMD, slightly lower mean austenite fraction, UTS, UE and YS (1838 ± 52 MPa, 7.3 ± 1.3% and 1363 ± 38 MPa), and also exhibits lower initial strain-hardening and much lower post-necking ductility. Fig. 5b presents the available high C variants in analogy. The almost completely martensitic reference specimens (grey) reach UTS of 2309 ± 33 MPa at UE of 7.0 ± 0.1% at divergent post-necking ductility. Similar to this reference, VMD variants like Globular HC (red) are shifted up towards 2197 ± 1 MPa and towards higher UE of 10.4 ± 0.0%, compared to the low C case. At the same time, TE is reduced systematically, while the Globular austenite fraction remains comparable to that of the LC variant. Banded specimens (green), containing significantly more austenite, showed earlier yielding at 1582 ± 79 MPa but reached much higher TE of 25.7 ± 5.2% at somewhat reduced UTS of 2106 ± 68 MPa. Generally, all VMD microstructures share a tendency for flat “dome-shaped” tensile curves that are reflecting a more gradual and consistent hardening response than found for the reference states. Fig. 5c shows that more advanced carbide dissolution (achieved after 3 s at 1200 °C, compared to 1 s), while promoting less than half as much austenite, results in superior properties across the board, most notably in terms of strength, strain-hardening and TE.

SEM fractography was employed to classify the fracture behaviour of the five types of microstructures under tensile loading conditions. Fig. 6 provides a SEM overview of the full sample cross-sections, corresponding to the microstructures shown in Fig. 4. Immediately obvious are the differences among the three VMD microstructures. Lamellar LC (a) exhibits severe faulting along prior austenite grain boundaries, Globular LC (b) shows pronounced necking and deep, frequently radial cracks. In case of Banded HC (c), the cracks are even more pronounced, but propagate only along the rolling/segregation planes. In all three cases, final rupture occurs in a ductile manner always involving pronounced dimples (see representative close-up of (b)). In case of the martensitic reference (d), cleavage dominates across a level fracture surface (see close-up

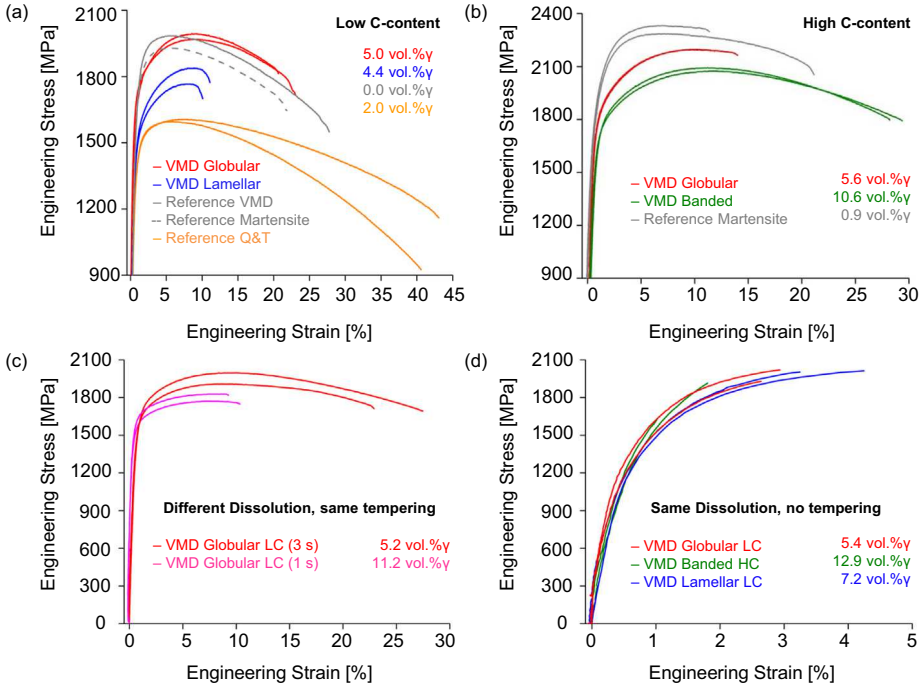

Fig. 5. DIC tensile curves for different microstructures and processing states (see Table 1), together with their mean XRD austenite fractions. The top row shows tempered microstructure comparisons at (a) low C-contents and (b) high C-contents, highlighting especially the impact of different vessel designed microstructures, as well as the difference in strain-hardening to reference structures. (c) compares the two previously characterised flash heated states (Fig. 2) after identical tempering for one microstructure, showing a pronounced difference and no correlation of ductility and austenite fraction. Lastly, (d) compares the three different VMD microstructures in the as-quenched state, in the absence of any tempering, still showing some ductility.

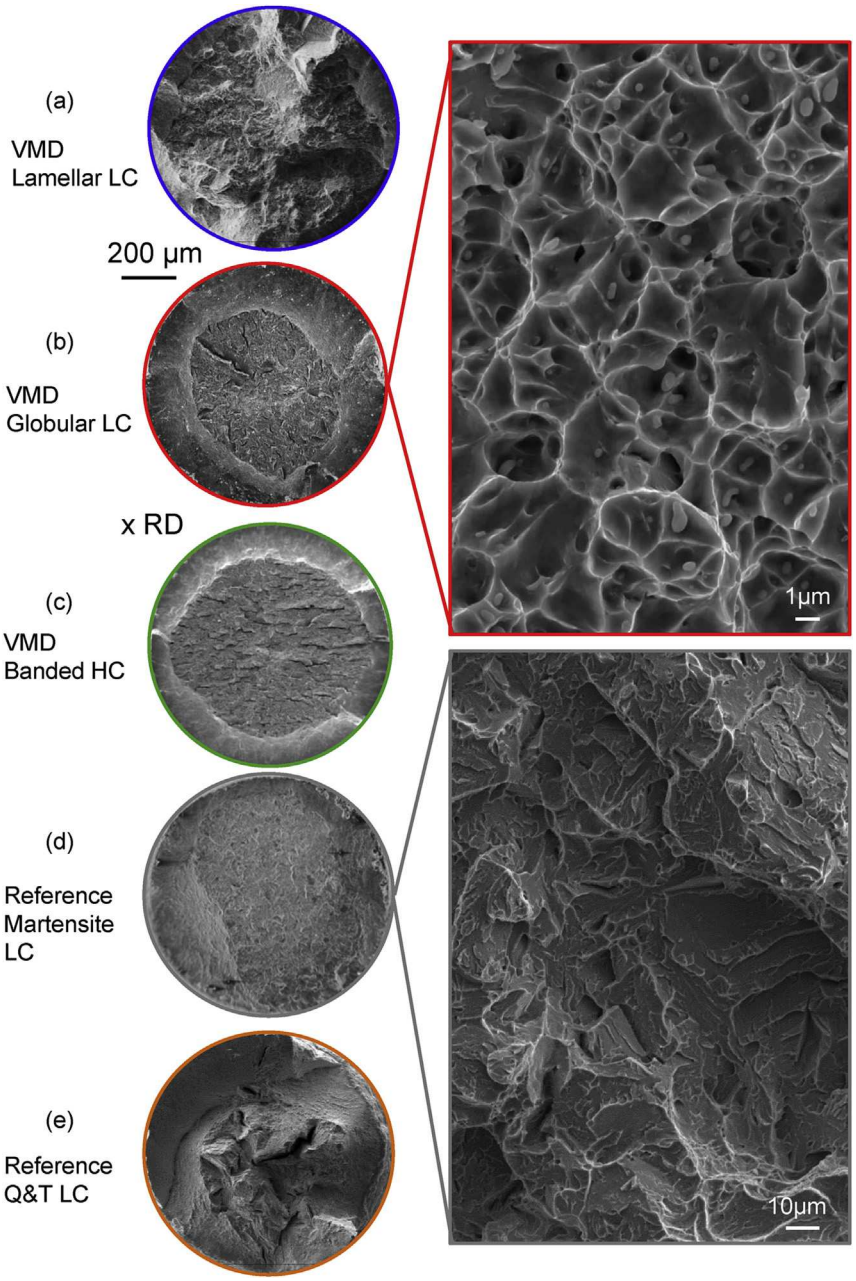

Fig. 6. SE fractography shows full tensile sample cross-sections after rupture. The different microstructures, as characterised before in Fig. 4, are seen to entail unique fracture surfaces already at this scale. On the micro-scale, VMD structures (a)-(c) are represented by a close-up of (b), showing ductile dimple fracture and residual carbides. Tempered martensite (d) is shown for reference, exhibiting cleavage fracture without pronounced dimples. The partitioned state (e) shows a mix of cleavage and dimple fracture.

of (d)). The reference state Q&T (e) shows large fracture facets and some evidence of cleavage can be found among the predominately dimple fracture zones.

A comprehensive performance profile of the examined microstructures and alloys is compiled in Fig. 7 for (a) low C and (b) high C microstructures, where the three VMD microstructures are compared to reference martensite and reference Q&T states (see Table 1). Apparently, all types of applied VMD processing pathways lead to a significant delay in necking, producing significantly higher uniform elongations than the reference samples, regardless of the chosen morphology, even though it still plays a critical modulating role, especially regarding strength and post-necking ductility. The micro-hardness, like the UTS, is comparable between VMD microstructures and reference monolithic martensite, being 527 ± 19 HV (LC) and 540 ± 19 HV (HC), in case of Banded the latter is even exceeded with 557 ± 35 HV.

Besides tensile strength and ductility, impact toughness is an important microstructural benchmark, especially critical in high strength steels. Evaluating this characteristic on dilatometer specimen was not possible due to the minimum sample size required. Flash heating was thus applied in different intensities by selected immersion times in a liquid Sn bath. Fig. 8 presents the 15 J impact toughness (blue squares) for Globular LC in relation to immersion time, normalised by the fractured area of 9 mm^2. As a reference, to account for the custom specimen geometry, a commercial X50CrMoV15 blade steel (as-delivered condition, 22 vol.% austenite) reached 3.2 ± 0.5 J at 544 ± 12 HV. For all VMD states, micro-hardness (red triangles) and XRD austenite fraction (green

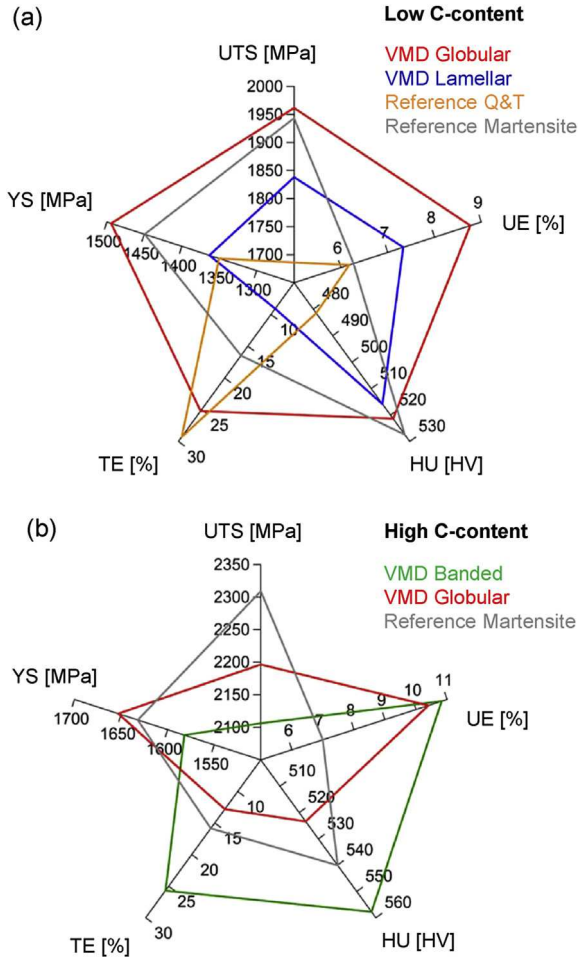

Fig. 7. Radar plots, compiling the mean values of tensile properties determined, averaged over all respective VMD and reference samples, for (a) low C-contents and (b) high C-contents. The HV values given are averaged over at least 400 micro-hardness indents obtained from several samples. YS: Off-set yield strength, UTS: Ultimate tensile strength, UE: uniform elongation, TE: total elongation to fracture, HU: micro-hardness.

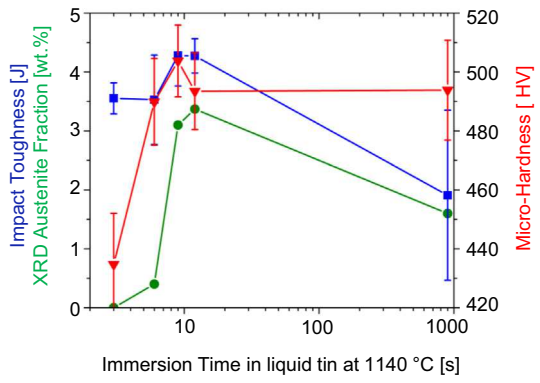

Fig. 8. The evolution of micro-hardness, XRD austenite fraction and 15 J impact toughness, normalised to 9 mm^2, as measured for Globular LC material with progressing carbide dissolution, which was achieved by varied immersion times in liquid Sn. Results show a surprising correlation of hardness and toughness, forming a slight optimum together with the austenite fraction towards the early stage of carbide dissolution.

circles) evolution is tracked additionally, measured post-mortem perpendicular to the impact direction. As high temperature exposure is increased for the VMD states, both, hardness and toughness rise, the former then plateaus while the latter drops significantly. The austenite fraction, though consistently low in case of this heat treatment, develops in sync with the toughness and, surprisingly, to some extent also with the hardness.

5. Discussion

The VMD approach successfully produced three novel types of microstructures, all of which comprise austenite shells, retained around partially dissolved carbides of tailored shapes and sizes. While modulated by the individual carbide morphology, these core-shell-type microstructures all show generally attractive mechanical properties, especially after posterior tempering at 200 °C. Strategically, applying such a relatively mild tempering is critically important in order to limit martensite softening, made possible in this case due to having produced martensitic-austenitic steel based on "primary" retained austenite. Unlike with the more conventional "secondary" austenite stabilised by Q&T [8,14] or Q&P [3,10] only after an initial quench, no partitioning at elevated temperatures is required in case of VMD. Moreover, employing vessel carbides allows to stabilise significant fractions of up to 11 vol.% of retained austenite at 0.2 wt.% C, an achievement not matched by the also applied conventional partitioning treatment (reference Q&T), where (transition) carbide precipitation acts as a competing influence [8,16] and, due to the low M_S temperature, only 2 vol.% of austenite could be achieved to no significant benefit of the UE. For comparison, even at 0.3 wt.% C, only 8 vol.% of austenite can be expected after partitioning at 400 °C [26]. While this fraction may be increased further by a carefully optimised Q&P treatment [13], a significant strength reduction (to below 1600 MPa) is nonetheless incurred during any such partitioning treatment, as is well reflected by the investigated Q&T reference material (Fig. 5a). In the present case, results obtained by DIC tensile testing, fractography and impact toughness specifically show that the application of VMD processing imparts significant improvements, especially to the safe tensile strain (UE, Fig. 5) and fracture energy (Figs. 6 and 8), while preserving the ultra-high strength levels attained by conventionally tempered reference martensite. In agreement, impact toughness results (Fig. 8) show the improvement of fracture resistance at only a negligible cost to overall hardness, which may even be increased by the contribution of carbides (Fig. 7b). Overall tensile ductility is even increased in the as-quenched condition (Fig. 5d), in which martensite devoid of alloy carbides fails in the elastic regime [26].

From the pronounced differences to reference states, as well as from the array of properties attainable through different carbide morphologies and dissolution states (Fig. 5a, c), it is clear how drastically a redistribution of chemical elements can alter and improve the mechanical property profile within one single alloy. The likely mechanisms, by which the chemical gradients may achieve these improved properties, for which they are ostensibly responsible, are either the TRIP-effect brought on by the chemical stabilisation of austenite, or a composite-effect induced by the core-shell particles themselves. The presence of carbides is known to enhance the extent of grain refinement induced by flash heating (Fig. 4), which reportedly benefits both, UTS and TE [35], as well as YS after Hall-Petch [36], but is unlikely to improve UE [37], and may not explain the difference to reference states on its own. Furthermore, the prior austenite grain size is not uniform throughout the three VMD microstructures (Fig. 4) while the strain-hardening behaviour is in principle comparable (Fig. 5). Hence, the main cause of this behaviour is likely not found in grain refinement, but elsewhere. The UE was chosen as the main parameter to gauge the acting strain-hardening mechanism and thus the extent to which strain localisation is delayed, being the preferred measure of

effective and safe ductility. This distinction from general ductility is especially important since the custom tensile sample geometry may lead to an overestimation of the total elongations [10,38], while having little effect on strength [38].

5.1. Austenite transformation

Compared to the reference microstructures, the presence of the higher, but still comparatively low, austenite fractions attained by VMD (5.4–10.0 vol.%, depending on C-content), correlates with improved strain-hardening behaviour and affiliated rise in uniform elongations (by up to 3.0 and 3.8% for Granular LC and Banded HC, respectively). Thus, the delay of necking achievable by VMD processing, clearly exceeds the theoretical best case prediction for TRIP-assisted ductility increase, predicted to be at most 2.3% for the range of 5–15 vol.% austenite [39].

For clarifying the role of TRIP-assisting austenite in the novel core-shell microstructures, results of further study into the deformation phenomena are compiled in Fig. 9. The EBSD measurements in Fig. 9a are based on full cross-sections of Globular LC samples prepared after interrupted tensile tests. From left to right, the deformation states conform to the unloaded condition (measured within the thread, see Fig. 1b), the early plastic regime (YS for this specimen was 1488 MPa), and to the necking regime (UE for this specimen was 9.5%). It can be seen that the austenite fraction decreases with straining, but persists into the necking regime. Furthermore, the core-shell austenite seems to diminish in thickness and partially disappears from the adjoining carbide surfaces with increasing strain. Thus, a gradual transformation at the level of individual grains is indicated, constituting an incremental evolution in contrast to the conventional "burst-like" transformation of individual austenite grains, which only appears gradual when averaged across the whole austenite population [40]. To the author's knowledge, examples of a similarly gradual transformation have otherwise been found only in lean maraging TRIP/TWIP steels, in the presence of ε-martensite, where transformation was related to twinning [5]. However, these conditions are not comparable to the present case, in which no intermediate ε-martensite was observed and α′-martensite should form directly, through shear [41].

The character of the respective VMD microstructures' deformation induced transformation of austenite can be analysed in a number of ways [3,23,42], of which the Burke-Matsumura (B-M) model [23] was selected in the present case. This model, applicable for similar C-contents and a variety of XRD austenite fractions [23,42,43], consists of an adapted diffusional kinetics model of isothermal austenite decomposition, replacing elapsed time by the monotonically increasing strain. In so doing, the fitting parameters p and k then empirically describe the austenite transformation kinetics in terms of its autocatalytic tendency and its thermodynamic driving force or stability, respectively [23]. Fig. 9b provides an overview over austenite fractions found after interrupted tensile tests by XRD (filled symbols, mean values) and EBSD (open symbols), for the three microstructures from Fig. 5. In Table 2, published

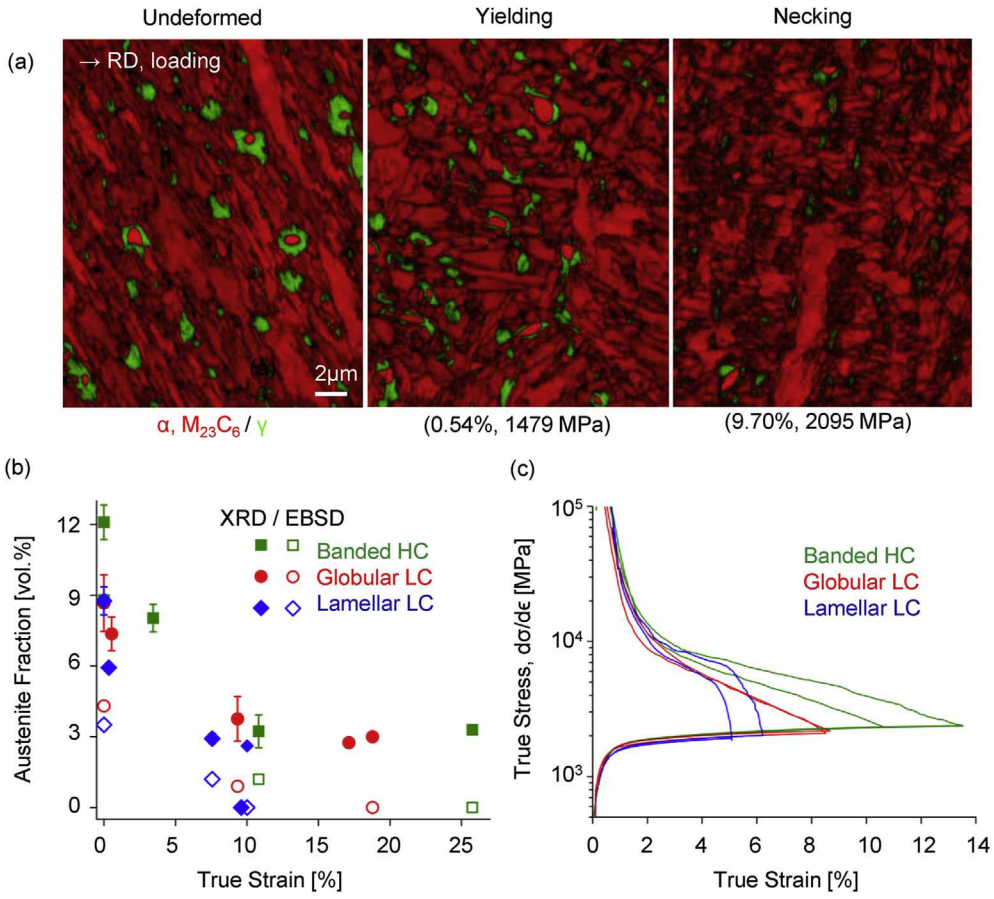

Fig. 9. (a) EBSD mappings of interrupted DIC tensile tests correlate strain with austenite content, showing a gradual decline in the thickness of austenite shells and their incremental disappearance. (b) Austenite transformation kinetics with strain according to measurements by EBSD and by XRD (averaged values) for the three VMD microstructures. The larger values determined by XRD are expected to result from a larger probed volume and a reduced effect of the free surface as compared to EBSD. (c) True stress-strain curves and strain-hardening rates dσ/dε representative of these microstructures.

Table 2
Tabulated comparison of Burke-Matsumura model data, in the form of fitting parameters *p* and *k*, describing the kinetics of the TRIP-effect, for published data of conventional alloys and that derived from VMD microstructures, as presented in Fig. 9, for comparable austenite fractions. The parameters *k* and *p* represent driving force of austenite transformation and its proclivity for autocatalytic transformation, respectively.

Microstructure	XRD austenite fraction [wt.%]	k-value	p-value
Austempered TRIP	12.0	94	1
Matsumura et al.[23]	16.9	25	1
	17.1	33	1
	17.5	64	1
	19.2	52	1
Quenched and Partitioned (Q&P)	7.7	16	0.52
De Moor et al. [43]	11.2	33	0.71
	14.8	120	1.17
VMD Lamellar LC	4.7	81	0.85
VMD Globular LC	6.8	54	0.69
VMD Banded HC	9.1	36	0.47

data of conventional Q&P and austempered TRIP steels, along with the relevant austenite fractions, is compared with the B-M model statements on VMD austenite stability. Generally, the stability indicators *p* and *k* derived for VMD are comparable in magnitude to those of established TRIP-assisted steels [23,43], lending further credence to the assumption of TRIP-assisted strain-hardening in the present case. Moreover, while, with increasing austenite fractions, Q&P steels naturally (due to the austenite fraction being inversely proportional to its C-content [16], which determines their stability) show an increased proclivity for autocatalytic martensite formation (*p*-values) as well as a higher driving force (*k*-values) to this effect, the case is different for VMD specimens. There, as also with austempered TRIP steels [44], auto-catalytic transformation is thought to be counteracted by the nodular and insulated austenite, as opposed to the monolithic colonies of inter-lath austenite typically associated with partitioning [17,33].

Furthermore, unlike with Q&P, the VMD austenite C-content is not directly related to its volume fraction, but instead depends in a complex manner on the chemical gradients as they were imposed during carbide dissolution [26]. In turn, the distribution, shape and scale of these chemical gradients naturally are a consequence of the underlying carbide dispersion [27] and, therefore, the choice of processing parameters.

To highlight this effect, Fig. 9c compares the three chief microstructures (red: Globular LC, blue: Lamellar LC, green: Banded HC), finding that, in case of the elongated/lamellar core-shell particles, the change in strain-hardening is most pronounced and only there a clear inflexion point, indicative of TRIP-hardening [45], is exhibited. The relatively subtle change in strain-hardening rate of other VMD samples may be related to the small amount of austenite present, combined with its gradual nature of transformation, but also the much stronger matrix, if compared to conventional TRIP-steels.

While showing the strongest change in hardening rate in this manner, the Lamellar VMD condition is, at the same time, linked with the earliest necking as well as the lowest TE. Both the distinctive drop in strain-hardening rate and the early failure may be explained by the frequently coarse and elongated carbides (Fig. 2a) and the resultant rise of stress concentration factors [46], thus projecting the highest driving force for abrupt austenite transformation in Lamellar LC microstructures, as is reflected by its higher k- and *p*-values (Table 2). The low yield strength in this case is likely caused by heterogeneous yielding imposed by inhomogeneous carbide distribution and size, which would also explain the low post-necking ductility through easy and early delamination (loss of matrix-carbide cohesion at sharp tips). By contrast, the offset yield strengths are consistently very high for the Globular VMD materials, irrespective of applied tempering (Fig. 3) or C-content (Fig. 7). This late yielding, even compared to the reference state of monolithic martensite, should be related to the significant refinement of the martensitic matrix (compare IPF, Fig. 4), well known to be induced by flash heating [47], most notably for the type of fine carbide dispersion presented in case of the Globular samples. In addition to the yield point, structure refinement may also serve to increase hardness and strength [35], but this does not fit to them decaying with tempering (Fig. 3). In any case, the combination of high yield strengths with significant strain-hardening reserves allows at least the Globular LC microstructure to overcome the general principle of inverse strength and ductility relationship by measuring up to martensite in the former and surpassing it in the latter (Fig. 5a). The overall highest ductility of VMD states, however, was achieved in the Banded variant, regardless of its comparably higher C-content. According to literature, such a banded arrangement of austenite along the tensile axis should be detrimental to austenite stability and fracture resistance [48]. However, these contradicting results were obtained under the simulation condition of a soft ferritic matrix, whereas in the present case the much stronger martensite may be load-bearing, thus shielding the austenite fraction. Another factor could be the laminate structure of martensite itself, which is periodically varying in C-content and hardness, both being highest in the vicinity of the stacked carbide-austenite planes (Fig. 6). In this sense, the Banded VMD variant can be regarded as a composite structure not only microscopically (core-shell particles) but also macroscopically (segregation planes inducing perpendicular hardness gradients, in a “sandwich” structure). Thus, while post-mortem phase quantification by EBSD and XRD, as well as the B-M model comparison, speak for a significant contribution to strain-hardening by the TRIP-effect, there remains the influence of composite interactions.

5.2. Core-shell composites

Besides mechanically-induced austenite transformation, another way to explain the VMD tensile properties is by the composite nature inherent to the underlying three-phase laminates. It is the dynamic interplay, or “strain-partitioning” [49], between phases that may affect strain-hardening phenomena on the local level, on top of possible macroscopic composite effects as were proposed for the Banded variants (“sandwich structure”). Beyond imposing graded austenite stability along the submicron-scale [26], the chemical gradients emanating from dissolving carbides can also be expected to mould the elastic/plastic response of the entire microstructure, as sketched exemplarily for one such core-shell particle in Fig. 10a. The sketch shows the case of continuous enrichment gradient in Cr and C, as characterised elsewhere [26], in conjunction with how mechanical properties like stiffness (Young’s modulus) and strength (nano-hardness) may be expected to vary along the chemical gradient in Cr and C that is surrounding the

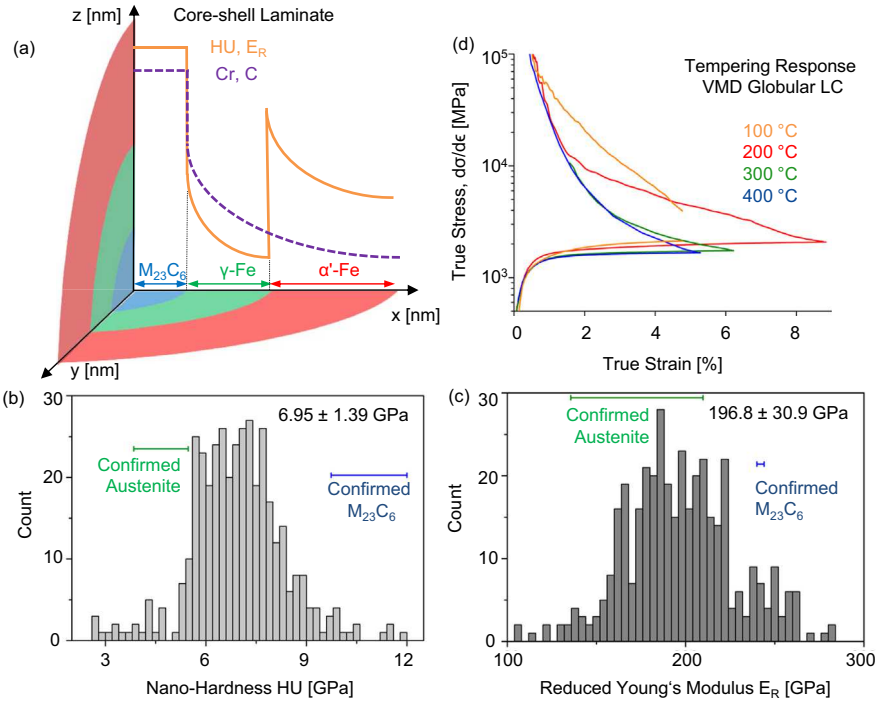

Fig. 10. (a) Sketch of how the chemical gradients (purple) around carbides are related to phase stability and how they are expected to induce mechanical gradients (orange) in hardness and stiffness, producing a micromechanical core-shell laminate. The histograms below show the results of correlative nano-indentation performed on VMD Globular LC material to detect such graded properties in the form of (b) nano-hardness (HU) and (c) reduced Young's modulus (E_R). Range bars denote mean and standard deviations of points that could be confirmed by SEM/EBSD as carbides or austenite, respectively. (b) nano-hardness (HU) and (c) reduced Young's modulus (ER). Range bars denote mean and standard deviations of points that could be confirmed by SEM/EBSD as carbides or austenite, respectively. A wide range of values is indicated for both hardness and stiffness, which is also reflected by the total mean and standard deviation of all phases combined, shown to the top right of the respective histograms. (d) True stress-strain curves and strain-hardening rates highlighting the temper response of the same microstructure and showing again the optimum property profile only after mild tempering at 200 °C. (For interpretation of the references to colour in this figure legend, the reader is referred to the web version of this article.)

carbides, reaching considerable enrichment factors of approximately 1.8 in both elements [26]. To gain insight into the range of these mechanical properties, correlative nano-indentation was applied, in which characterisation by SE-imaging and EBSD, both prior to and after indentation, allowed a correlation of phase constituents and mechanical data. Thus, at least a partial quantification of the core-shell microstructure in terms of average constituent properties was possible, of which reduced Young's modulus (E_R) and nano-hardness (HU) are presented as histograms in Fig. 10b and c.

The residual $M_{23}C_6$ carbides were found to have a near uniform hardness of 10.9 ± 1.1 GPa (standard deviation, three confirmable indents), agreeing well with literature values [50]. The austenite shells, expected to show a graded hardness, due to local chemical gradients [26], were measured at 4.7 ± 0.8 GPa, averaged over 15 confirmed indents, loading-induced transformation being ruled out by EBSD correlation. In analogy, the reduced elastic modulus ranges from 242.0 ± 1.8 GPa for carbides to 172.7 ± 37.1 GPa for austenite. These measurements show a wide distribution of values, spanning almost 100–300 GPa in modulus and more than 3–12 GPa in hardness. In terms of the confirmed austenite subset, there is good agreement of mean values with comparable measurements of a more highly alloyed 18Cr–8Ni stainless steel [51], albeit with VMD austenite presenting a much wider range. While joint loading of phases was carefully checked and ruled out on the surface, resolution limits and 3D-effects are still likely sources of error. Nonetheless, using this correlative method, mean values could be affixed to the core-shell composite constituents sketched in Fig. 10a, as well as the considerable overall range of properties demonstrated.

Considering the implication of spatially graded stiffness and hardness during the onset of plastic deformation, yielding may be expected to commence and initially concentrate within the depleted martensite matrix, then progress (from right to left in Fig. 10a) in the course of work-hardening to the harder, more C-enriched martensite as well as, finally, to the enclosed austenite. Such a development would conform to dynamic strain-partitioning [49] and serve as an additional explanation for the observed gradual hardening behaviour of VMD microstructures (Fig. 5), on top of the TRIP-effect (Fig. 9) and in spite of their refined grain size (Fig. 4). Moreover, even after complete transformation of an austenite shell into martensite, a concentric slope in martensite hardness around the carbides would remain, owing to the chemical gradient (purple in Fig. 10a), which should counteract strain localisation leading to void formation and growth. Thus, such a type of laminate structure may also help explain the higher than predicted benefit of metastable austenite in the case of VMD microstructures. This laminate effect would tend to be more effective with spherical carbides and less so with coarse lamellar ones, which is corroborated by tensile data (Fig. 5a).

5.3. Posterior tempering

The tempering response of steel, even when only considering monolithic martensite, is a complex process in which the formation, pinning and degradation of dislocation substructures in combination with C-ordering and carbide precipitation, as well as release of thermal stresses, determine the attainable bulk mechanical properties [52]. In the case of VMD microstructures, the tempering response is furthermore complicated by being as well modulated locally by enrichments in alloying elements. While the austenite fractions seem little affected (Fig. 3), and its low diffusivity as well as high Cr-content and lowered C-activity should

serve to preserve its existing C-gradients, the surrounding martensite should be subject to significant change with tempering (Fig. 3).

As a result, for different temper intensities the composite effect, as visualised in Fig. 10a, is modified strongly, correlating with a change in strain-hardening behaviour, as presented in Fig. 10b. Whereas after 100 °C tempering the material remains overwhelmingly brittle, an optimum state is reached after 200 °C, characterised by an initially lower, but later more gradually persisting, strain-hardening rate. This effect at higher strains is lost with increasing temperature and hardening becomes almost uniform for 300 and 400 °C. The effects of such over-tempering are higher post-necking elongations, but also significantly lower UE. As the delayed necking found only after optimal tempering was related to both the TRIP-effect and beneficial strain-partitioning, so is its loss after excessive tempering likely is linked with their decline. It seems likely that a lower and overall more uniform martensite hardness would promote earlier yielding (Fig. 3) and thereby transfer more stress to the retained austenite, prompting its earlier and less beneficial transformation into martensite, which would accelerate transformation of the remaining austenite even further [3]. Additionally, the replacement of transition carbides by cementite within martensite may also negatively influence the mechanical properties [53].

More study is needed to better understand and document the complex interactions of microstructure parameters and chemical gradients with tempering processes.

6. Conclusions

The core-shell particles, consisting of hard carbides, coated in ductile austenite, embedded within a strong martensitic matrix, are at the heart of the VMD steel microstructures and their improved ductility at ultra-high strength. The carbides also enable significant refinement of the prior austenite grain size and thus of the martensite structure. The vessel carbides also impose self-organising chemical gradients upon their partial dissolution which enable the retention of significant fractions of TRIP-assisting austenite, in controlled morphology and size, and are considered to also induce a periodically graded hardness and stiffness throughout the thus tailored microstructures and offering opportunities for beneficial strain-partitioning as a function of tempering. The following conclusions can be drawn:

1) VMD processing was demonstrated to induce spectacular mechanical properties, considering the lean alloys compositions examined, with mean ultimate tensile strengths in excess of 2.0 and 2.2 GPa at uniform elongations of 9 and 10% being reached.
2) The carbide-ferrite microstructures, easily modifiable prior to carbide dissolution, enable a wide range of austenite morphologies and associated tensile properties. A homogeneous distribution of globular carbides was indicated to be most favourable in terms of yield and tensile strengths. A banded arrangement of both carbides and austenite was observed to be most ductile and fracture resistant.
3) Within individual core-shell particles, mechanical austenite-to-martensite transformation appears to progress gradually with increasing strain, offering an ideal and consistent benefit up to the necking regime. Macroscopically, this process is in line with reported transformation kinetics of conventional TRIP-assisted steels.
4) Hardness and strength were not found to be negatively affected by the inclusion of only 5 to 10 vol.% of austenite. The inclusion of austenite is compensated for by significant structural refinement of the martensite matrix through flash heating as well as by the hardness contribution of carbides.
5) Unlike C-partitioning, resulting in a bimodal combination of evenly enriched austenite and fully depleted martensite, VMD processing produces chemically as well as mechanically graded laminates with superior properties, achievable for a wide range of alloys. This is made possible by relying on quasi-stoichiometric carbide vessels to supply local alloying, instead of being limited by bulk alloy composition or M_S temperatures. In particular, the tensile strength can be scaled by C-levels without strongly affecting either austenite fraction or ductility.

The potential for a further optimisation of processing parameters was clearly shown, both for posterior tempering where the existence of a clear optimum was shown, as well as for carbide dissolution, which when varied showed a surprising correlation of impact toughness with both hardness and the austenite fraction. Future work will focus on this critical flash-heating stage and how it may be adapted and made more readily accessible by transfer to a less temperature-stable vessel phase, such as cementite, or by alloying additions such as molybdenum and vanadium.

References

[1] E. Jimenez-Melero, N.H. van Dijk, L. Zhao, J. Sietsma, S.E. Offerman, J.P. Wright, S. Van der Zwaag, Characterization of individual retained austenite grains and their stability in low-alloyed TRIP steels, Acta Mater. 55 (2007) 6713–6723.
[2] E.V. Pereloma, A.A. Gazder, I.B. Timokhina, Addressing retained austenite stability in advanced high strength steels, Mater. Sci. Forum 738 (2013) 212–216.
[3] D. De Knijf, R. Petrov, C. Föjer, L.A. Kestens, Effect of fresh martensite on the stability of retained austenite in quenching and partitioning steel, Mater Sci. Eng. A 615 (2014) 107–115.
[4] V.F. Zackay, E.R. Parker, D. Fahr, R. Busch, The enhancement of ductility in high-strength steels, ASM Trans. Quart. 60 (1967) 252–259.
[5] M.-M. Wang, C.C. Tasan, D. Ponge, A. Kostka, D. Raabe, Smaller is less stable: size effects on twinning vs. transformation of reverted austenite in TRIP-maraging steels, Acta Mater. 79 (2014) 268–281.
[6] Z.J. Xie, Y.Q. Ren, W.H. Zhou, J.R. Yang, C.J. Shang, R.D.K. Misra, Stability of retained austenite in multi-phase microstructure during austempering and its effect on the ductility of a low carbon steel, Mater. Sci. Eng. A 603 (2014) 69–75.
[7] N.C. Goel, J.P. Chakravarty, K. Tangri, The influence of starting microstructure on the retention and mechanical stability of austenite in an intercritically annealed-low alloy dual-phase steel, Metall. Trans. A 18 (1987) 5–9.
[8] L. Yuan, D. Ponge, J. Wittig, P. Choi, J.A. Jiménez, D. Raabe, Nanoscale austenite reversion through partitioning, segregation and kinetic freezing: example of a ductile 2GPa Fe–Cr–C steel, Acta Mater. 60 (2012) 2790–2804.
[9] P. Jacques, Q. Furnémont, T. Pardoen, F. Delannay, On the role of martensitic transformation on damage and cracking resistance in TRIP-assisted multi-phase steels, Acta mater. 49 (2001) 139–152.
[10] B.C. De Cooman, Structure–properties relationship in TRIP steels containing carbide-free bainite, Curr. Opin. Solid State Mater. Sci. 8 (2004) 285–303.
[11] J. Speer, D.K. Matlock, B.C. De Cooman, J.G. Schroth, Carbon partitioning into austenite after martensite transformation, Acta Mater. 51-9 (2003) 2611–2622.
[12] T. Tsuchiyama, J. Tobata, T. Tao, N. Nakada, S. Takaki, Quenching and partitioning treatment of a low-carbon martensitic stainless steel, Mater. Sci. Eng. A 532 (2012) 585–592.
[13] J. Mola, B.C. De Cooman, Quenching and partitioning (Q&P) processing of martensitic stainless steels, Metall. Mater. Trans. A 44 (2013) 946–967.
[14] H. Springer, M. Belde, D. Raabe, Bulk combinatorial design of ductile martensitic stainless steels through confined martensite-to-austenite reversion, Mater. Sci. Eng. A 582 (2013) 235–244.
[15] K. Zhang, M. Zhang, Z. Guo, N. Chen, Y. Rong, A new effect of retained austenite on ductility enhancement in high-strength quenching–partitioning–tempering martensitic steel, Mater. Sci. Eng. A 528 (2011) 8486–8491.
[16] D.V. Edmonds, K. He, F.C. Rizzo, B.C. De Cooman, D.K. Matlock, J.G. Speer, Quenching and partitioning martensite – a novel steel heat treatment, Mater. Sci. Eng. A 438 (2006) 25–34.
[17] M.J. Santofimia, L. Zhao, R. Petrov, C. Kwakernaak, W.G. Sloof, J. Sietsma, Microstructural development during the quenching and partitioning process in a newly designed low-carbon steel, Acta Mater. 59.15 (2011) 6059–6068.
[18] I.B. Timokhina, E.V. Pereloma, P.D. Hodgson, Microstructure and mechanical properties of C–Si–Mn (–Nb) TRIP steels after simulated thermomechanical processing, Mater. Sci. Technol. 17 (2001) 135–140.

[19] D. Edmonds, D. Matlock, J. Speer, The recent development of steels with carbide-free acicular microstructures containing retained austenite, La Metall. Ital. 1 (2011) 41–49.
[20] K. Davut, S. Zaefferer, The effect of size and shape of austenite grains on the mechanical properties of a low-alloyed TRIP steel, Steel Res. Int. 83 (2012) 584–589.
[21] D.Q. Bai, A. Di Chiro, S. Yue, Stability of retained austenite in a Nb microalloyed Mn–Si TRIP steel, Mater. Sci. forum 284 (1998) 253–262.
[22] E.V. Pereloma, I.B. Timokhina, M.K. Miller, P.D. Hodgson, Three-dimensional atom probe analysis of solute distribution in thermomechanically processed TRIP steels, Acta mater. 55 (2007) 2587–2598.
[23] O. Matsumura, Y. Sakuma, H. Takechi, TRIP and its kinetic aspects in austempered 0.4C–1.5Si–0.8Mn steel, Scr. Metall. 21 (1987) 1301–1306.
[24] J. Wang, S. Van Der Zwaag, Stabilization mechanisms of retained austenite in transformation-induced plasticity steel, Metall. Mater. Trans. A 32 (2001) 1527–1539.
[25] S. van der Zwaag, L. Zhao, S.O. Kruijver, J. Sietsma, Thermal and mechanical stability of retained austenite in aluminum-containing multiphase TRIP steels, ISIJ Int. 42 (2002) 1565–1570.
[26] M. Belde, H. Springer, G. Inden, D. Raabe, Multiphase microstructures via confined precipitation and dissolution of vessel phases: example of austenite in martensitic steel, Acta Mater. 86 (2015) 1–14.
[27] R.R. Judd, H.W. Paxton, Kinetics of austenite formation from a spheroidized ferrite-carbide aggregate, Trans. Metall. Soc. AIME 242 (1968) 206–214.
[28] D.V. Shtansky, Formation of austenite and dissolution of carbides in Fe–8.2Cr–C alloys, Z. Met. 90 (1999) 25–37.
[29] G. Miyamoto, H. Usuki, Z.-D. Li, T. Furuhara, Effects of Mn, Si and Cr addition on reverse transformation at 1073K from spheroidized cementite structure in Fe–0.6 mass% C alloy, Acta Mater. 58 (2010) 4492–4502.
[30] L. Lutterotti, S. Matthies, H.R. Wenk, MAUD (material analysis using diffraction): a user friendly java program for Rietveld texture analysis and more, in: Proceeding of the Twelfth International Conference on Textures of Materials (ICOTOM-12), NRC Press, Ottawa, Canada, 1999.
[31] C.F. Jatczak, Retained Austenite and its Measurement by X–ray Diffraction, Technical report, SAE Technical Paper, 1980.
[32] G. Krauss, Deformation and fracture in martensitic carbon steels tempered at low temperatures, Metall. Mater. Trans. A 32 (2001) 861–877.
[33] Y. Toji, H. Matsuda, M. Herbig, P.-P. Choi, D. Raabe, Atomic-scale analysis of carbon partitioning between martensite and austenite by atom probe tomography and correlative transmission electron microscopy, Acta Mater. 65 (2014) 215–228.
[34] Y. Toji, G. Miyamoto, D. Raabe, Carbon partitioning during quenching and partitioning heat treatment accompanied by carbide precipitation, Acta Mater. 86 (2015) 137–147.
[35] R.A. Grange, Strengthening steel by austenite grain refinement, ASM Trans. Quart. 59 (1966) 26–48.
[36] M. Calcagnotto, D. Ponge, D. Raabe, Effect of grain refinement to 1μm on strength and toughness of dual-phase steels, Mater. Sci. Eng. A 527 (2010) 7832–7840.
[37] T. Furuhara, K. Kikumoto, H. Saito, T. Sekine, T. Ogawa, S. Morito, T. Maki, Phase transformation from fine-grained austenite, ISIJ Int. 48 (2008) 1038–1045.
[38] Y.H. Zhao, Y.Z. Guo, Q. Wei, A.M. Dangelewicz, C. Xu, Y.T. Zhu, E.J. Lavernia, Influence of specimen dimensions on the tensile behavior of ultrafine-grained Cu, Scr. Mater. 59 (2008) 627–630.
[39] H.K.D.H. Bhadeshia, TRIP-assisted steels? ISIJ Int. 42 (2002) 1059–1060.
[40] Y. Matsuoka, T. Iwasaki, N. Nakada, T. Tsuchiyama, S. Takaki, Effect of grain size on thermal and mechanical stability of austenite in metastable austenitic stainless steel, ISIJ Int. 53.7 (2013) 1224–1230.
[41] H.K.D.H. Bhadeshia, R.W. Honeycombe, Steels: Microstructure and Properties: Microstructure and Properties, third ed., Butterworth-Heinemann, Oxford, 2011.
[42] P.J. Gibbs, E. De Moor, M.J. Merwin, B. Clausen, J.G. Speer, D.K. Matlock, Austenite stability effects on tensile behavior of manganese-enriched-austenite transformation-induced plasticity steel, Metall. Mater. Trans. A 42 (2011) 3691–3702.
[43] E. De Moor, S. Lacroix, A.J. Clarke, J. Penning, J.G. Speer, Metall. Mater. Trans. A 39A (2008) 2568–2595.
[44] L. Samek, E. De Moor, J. Penning, B. De Cooman, Influence of alloying elements on the kinetics of strain-induced martensitic nucleation in low-alloy, multiphase high-strength steels, Metall. Mater. Trans. A 37 (2006) 109–124.
[45] C. Herrera, D. Ponge, D. Raabe, Design of a novel Mn-based 1GPa duplex stainless TRIP steel with 60% ductility by a reduction of austenite stability, Acta Mater. 59 (2011) 4653–4664.
[46] M. Huang, Z. Li, Influences of particle size and interface energy on the stress concentration induced by the oblate spheroidal particle and the void nucleation mechanism, Int. J. Solids Struct. 43 (2006) 4097–4115.
[47] R.A. Grange, The rapid heat treatment of steel, Metall. Trans. 2 (1971) 65.
[48] J. Shi, S. Turteltaub, E. Van der Giessen, Analysis of banded morphology in multiphase steels based on a discrete dislocation–transformation model, Model. Simul. Mater. Sci. Eng. 19 (7) (2011) 074006.
[49] M.-M. Wang, C.C. Tasan, D. Ponge, A.-Ch Dippel, D. Raabe, Nanolaminate transformation-induced plasticity-twinning-induced plasticity steel with dynamic strain partitioning and enhanced damage resistance, Acta Mater. 85 (2015) 216–228.
[50] A. Inoue, S. Arakawa, T. Masumoto, Effect of alloying elements on defect structure and hardness of M23C6 type carbides, Trans. Jpn. Inst. Metals 20 (1979) 585–592.
[51] L. Qian, M. Li, Z. Zhou, H. Yang, X. Shi, Comparison of nano-indentation hardness to microhardness, Surf. Coat. Technol. 195 (2005) 264–271.
[52] G. Krauss, C.J. McMahon Jr., Low-toughness and Embrittlement Phenomena in Steels, Martensite, 1992, pp. 295–321.
[53] J.G. Speer, D.V. Edmonds, F.C. Rizzo, D.K. Matlock, Partitioning of carbon from supersaturated plates of ferrite, with application to steel processing and fundamentals of the bainite transformation, Curr. Opin. Solid State Mater. Sci. 8 (2004) 219–237.